JOURNAL OF MATERIALS SCIENCE 32 (1997) 6153–6162

Fracture process of thermally shocked discontinuous fibre-reinforced glass matrix composites under tensile loading

K. OGI*
Research Institute for Applied Mechanics, Kyushu University, 6-1 Kasuga-Koen, Kasuga City, Fukuoka 816, Japan

N. TAKEDA
Center for Collaborative Research, The University of Tokyo, 4-6-1 Komaba Meguro-ku, Tokyo 153, Japan

K. M. PREWO
United Technologies Research Center, East Hartford, CT 06108, USA

Fracture mechanisms of discontinuous carbon-fibre-reinforced glass matrix composites were experimentally studied for specimens with initial damage induced by thermal shock. First, matrix cracking due to thermal shock was observed using both optical microscopy and scanning acoustic microscopy (SAM) to reveal the damage state. Secondly, tensile stress–strain behaviour and acoustic emission during tensile tests were measured for specimens with and without thermal shock. The progress of microscopic damage during tensile loading was also investigated using both replica and *in-situ* SAM techniques. Finally, macroscopic transient thermal stresses during thermal shock were calculated using finite-element analysis. It is proved that the fracture process of the composite specimen with thermal-shock-induced cracks is different from that of the virgin specimen. This difference in fracture processes is attributed to the difference in the evolution of matrix cracking, which is affected by pre-existing microcracks in the matrix.

1. Introduction

Advanced ceramic materials are expected to be used as heat-resistant structural materials. However, the fracture toughness of these materials is so low that their application is very limited. Because of their brittleness, strength degradation easily occurs when they are subjected to mechanical or thermal impact loading. Therefore, ceramic matrix composites (CMCs) reinforced with whiskers or fibres have been investigated for the establishment of high-toughness materials.

Fracture process and mechanics of fibre-reinforced CMCs has been widely investigated by many researchers and reviewed by Evans and Zok [1]. Characterization of fracture process has been performed using some non-destructive technique. Damage evolution in silicon carbide (Nicalon)-fibre-reinforced calcium aluminosilicate (CAS) composites has been observed using the replication technique [2, 3]. *In-situ* observations using optical microscopy have been conducted for unidirectional and cross-ply Nicalon-CAS laminates [4–6]. The progress of damage in carbon–silicon carbide composites during tensile tests has been observed *in-situ* by scanning electron microscopy (SEM) [7]. Acoustic emission (AE) signals during loading have been measured for Nicalon-fibre-reinforced borosilicate glass (BSG) composites to monitor the fracture process [8, 9]. On the other hand, the thermal shock behaviour of fibre-reinforced CMCs has been studied for Nicalon–BSG and Nicalon–lithium aluminosilicate glass (LAS) [10], Nicalon–SiC [11, 12] and Nicalon–CAS [13]. In the previous work, the residual strength and modulus after thermal shock have been investigated; nevertheless, the fracture process of thermally shocked specimens during mechanical loading has not been characterized.

In 1982, Prewo [14] proved that randomly oriented discontinuous carbon fibre (CF)-reinforced BSG matrix composites shows a high compliance, a high failure strain and, accordingly, a high fracture toughness. The microfracture mechanics of this composite have been examined using AE measurement [15]. In the present study, two types of the above CF-BSG composites with and without initial cracks (plate 611 and plate 634, respectively) were employed. First, thermal-shock test were conducted for the virgin plate 634 specimen without initial cracks. Then, thermal-shock-induced damage was observed using optical

* Author to whom correspondence should be addressed.

0022–2461

microscopy and SAM. Secondly, tensile tests and AE measurement during tensile tests were conducted for the virgin plate 611, plate 634 and thermally shocked plate 634. Matrix cracking at each stress level was observed *in situ* by SAM during tensile loading [16] and was also optically observed using the replication technique. Finally, macroscopic transient thermal stress at the thermal shock is calculated by the finite-element method (FEM). The fracture mechanisms and processes of the CF-BSG composites were characterized through these experiments and observations.

2. Experimental procedure

2.1. Materials

The composites were fabricated (in United Technologies Research Center, East Hartford, CT) by the following procedure. Thin sheets of randomly oriented discontinuous CF paper (International Paper Company, Tuxedo Park, NY) were used for reinforcement of this composite. The initial mean fibre length was 19 mm before densification. The sheets were infiltrated with a slurry of BSG powder suspended in propanol. After drying, they were laid in a graphite die cavity for hot pressing. The CF–BSG plates of size 150 mm × 150 mm × 2–8 mm were hot pressed at 6.9 MPa pressure and temperatures above 1200 °C. The fibres were in a two-dimensional random array and separated from each other, although some fibre bundles were observed. The fibre volume fraction was 30–35% and the porosity was 1–3%.

The properties of the composite and constituent materials are summarized in Table I. Two significant features should be noted in this composite material. The first point is that the elastic modulus of the composite is smaller than that of the matrix (BSG), and the second is the large mismatch between the thermal expansion of the CF and the BSG matrix. These two points are related to fibre–matrix interfacial bonding and significantly affect the mechanical behaviour and the fracture mode of the CF–BSG, as will be discussed later.

Two composite plates, plate 611 and 634, were fabricated using different processing temperatures. Fig. 1 shows the SEM images of microstructures for the two composite plates. Plate 634 has some pores but no pre-cracks. Plate 611, on the other hand, had pre-existing microcracks randomly distributed in the matrix. Pre-cracks in plate 611 were introduced because of the slightly higher processing temperature.

2.2. Thermal shock tests

Plate 634 was cut into specimens of 150 mm × 5 mm × 3 mm size. The specimens were heated from room temperature to predetermined temperatures at a heating speed of 50 K min^{-1} in air using an infrared furnace (Fig. 2). After they were kept at these temperatures for 10 min to ensure temperature uniformity in the specimen, they were quenched in water (20 °C) to generate thermal-shock loading.

In order to estimate the heat transfer coefficient in water quenching, the time history of the temperature in the specimen was measured with the thermocouples embedded in the specimen. The value of the heat transfer coefficient was determined through the comparison between the experimental data and the result of finite-element analysis of transient heat condition.

2.3. Tensile tests and acoustic emission measurements

Fig. 3 shows the experimental set-up for a tensile test and AE measurement. Glass-fibre-reinforced epoxy doublers were adhesively bonded on the ends of the specimens. Tensile tests were conducted at a cross-head speed of 0.5 mm min^{-1} using an Instron 4204. The data acquisition system for load–strain measurement was controlled with a personal computer. Longitudinal strains were measured with the strain gauges on the specimen surface and the data were sent to the personal computer for further analysis. Two AE sensors (small wide-band sensor, PAC pico) were used and the AE data were analysed using a PAC 3000/3104 system. A preamplifier gain of 40 dB, a main gain of 20 dB and a threshold of 0.1 V were selected for data acquisition.

2.4. Microscopic observations

The faces and edges of the thermally shocked specimens were polished with diamond pastes of 9, 3 and 1 μm particle sizes in that order and microscopically observed using an optical microscope and scanning acoustic microscope (UH3, Olympus, Tokyo, Japan). In particular, SAM is suitable for the observation of microcracks with a small crack-opening displacement (COD) or fibre–matrix interfacial debondings. Matrix cracking with a small COD in plate 611 can also be detected using SAM.

In order to investigate the microscopic failure mechanisms, damage progress was observed using

TABLE I Properties of the composite and constituent materials

	Elastic modulus (GPa)	Density (g cm^{-3})	Thermal expansion (10^{-6} K)	Thermal conductivity (W m^{-2} K^{-1})	Specific heat (J kg^{-1} K^{-1})
Composite, in plane	52	2.09	1.7	> 1.04	752
Composite, normal to plane	28[a]		4.2	1.04	
Borosilicate	63	2.23	3.25		780
Celion, axial	234	1.76	− 0.5		670
Celion, radial			20		

[a] Calculated by measurement of the acoustic wave velocities.

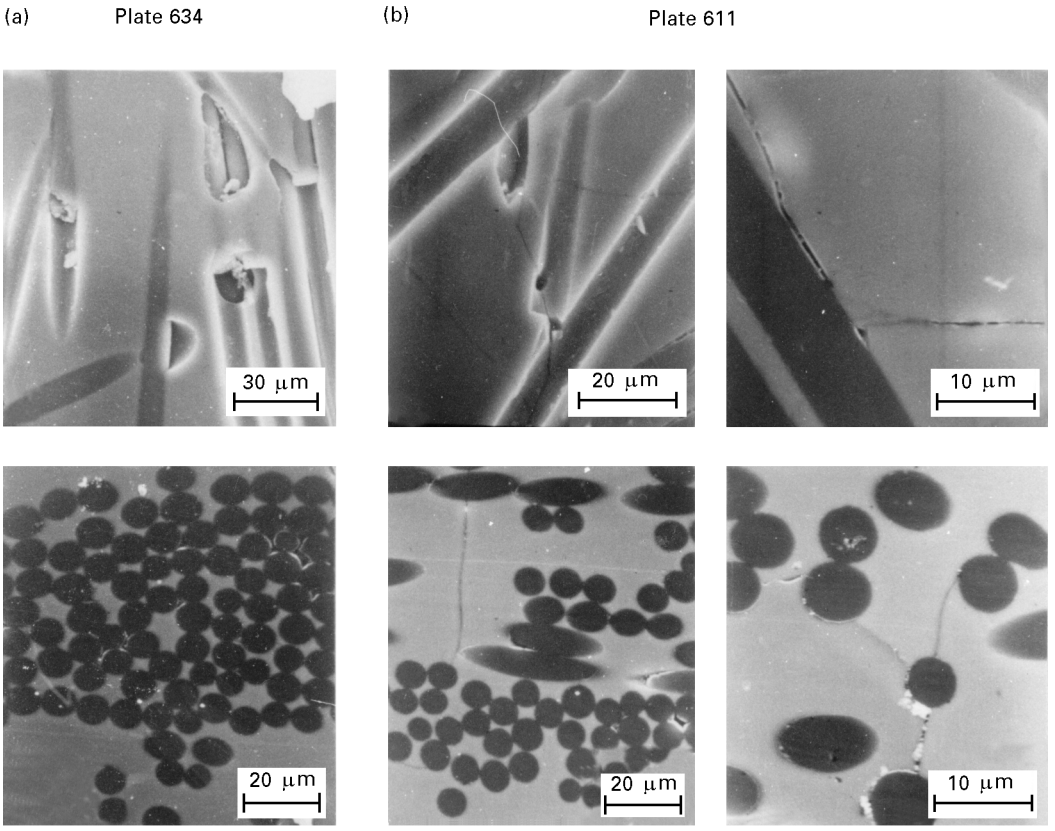

Figure 1 Scanning electron micrographs showing microstructures of (a) plate 634 and (b) plate 611. Some pre-cracks and pores can be seen in plate 634 and plate 611, respectively.

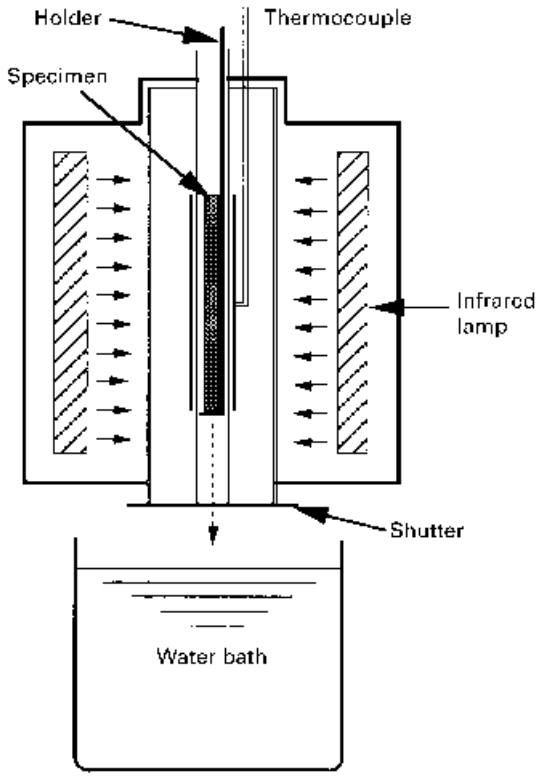

Figure 2 An infrared furnace for the thermal-shock test.

both replica and *in-situ* SAM techniques. Replicas of matrix cracking at each stress level were made by pushing the acetate films on the surface of the specimen subjected to tensile load. The propagation of matrix cracking on the films was observed using optical microscopy. In addition, tensile tests were conducted under SAM for more careful observation. Fig. 4 shows loading apparatus for *in-situ* SAM observation. This apparatus was mounted on the stage under the acoustic lens of the scanning acoustic microscope, and initiation and propagation of matrix cracking were microscopically observed while the specimen was loaded.

3. Thermal stress analysis

The macroscopic thermal stress at the thermal shock was analysed using the FEM. In order to reduce complications in the calculation, we assumed that first the heat transfer coefficient, h, is independent of time and temperature during thermal shock, secondly all the mechanical and thermal properties of the material are constant, and thirdly there is no heat generation inside the specimen and no heat radiation from the surface of the specimen. Fig. 5 illustrates the model for finite-element analysis. The analysis region (Fig. 5a) was limited to one quarter of the cross-sectional area of the specimen because of symmetry. Two-dimensional four-node plane-strain elements were selected in the present analysis. The quenching surfaces are AB and AD (Fig. 5b), where the constant heat transfer coefficient, h, is given. The material properties in Table I and the value of h estimated from the experimental data are employed in the analysis.

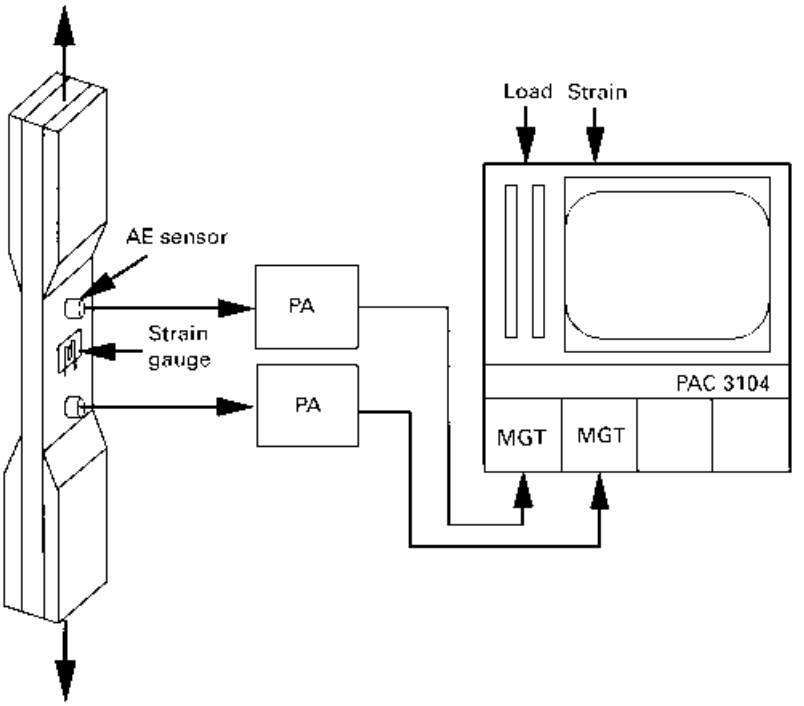

Figure 3 An experimental set-up for the tensile test and AE measurement. MG, main gain; T, threshold; PA, preamplifier.

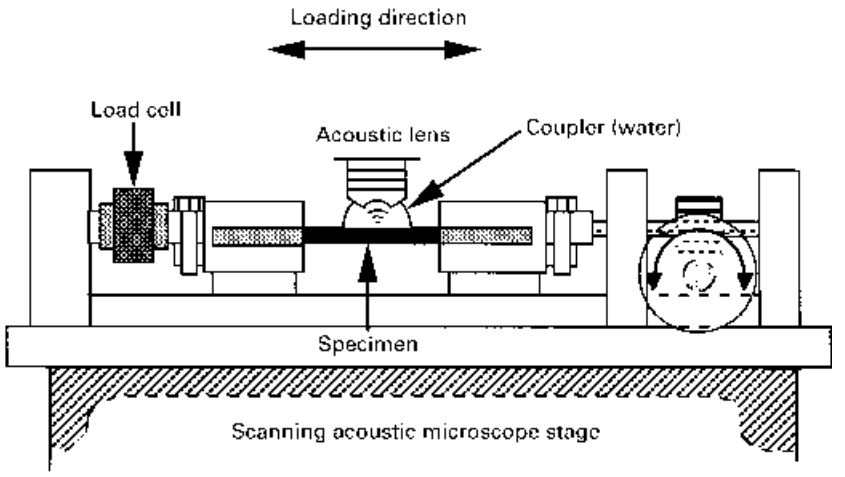

Figure 4 A loading apparatus for *in-situ* SAM observation.

4. Results

4.1. Microscopic observation of thermal-shock-induced damage

Fig. 6 shows optical micrographs of thermal-shock-generated matrix cracking for temperature differences ΔT of 530 and 600 K. Matrix cracking was observed near the surface and randomly distributed on the surface. Thermal-shock-induced crack densities are 0.2 cracks mm^{-1} for $\Delta T = 530$ K and 0.5 cracks mm^{-1} for $\Delta T = 600$ K. This leads to a decrease in elastic modulus as will be shown in the tensile test results.

Fig. 7 shows the matrix cracking observed by SAM. Using SAM, a crack is identified by multiple interference fringes parallel to the crack length when an incident acoustic wave is focused slightly under the surface, even if the COD is very small, such as 0.1 μm. In the present observation, the matrix cracking was detected up to the maximum depth of 250 μm from the surface.

4.2. Tensile tests and acoustic emission measurements

Fig. 8 indicates the tensile stress–strain curves for plate 611 and plate 634 (with and without thermal shock). Virgin plate 634 without thermal shock damage exhibits a distinctive non-linear stress–strain curve. There are the following three stages in this curve: stage I is the linear elastic stage (initial Young's modulus is 44.6 GPa); stage II is the plateau stage; stage III is the pseudo-"work-hardening" stage. This behaviour is attributed to matrix multiple cracking in stage II. That is, extensive matrix cracks with almost the same crack spacing are generated normal to the tensile direction through the specimen width [9, 10].

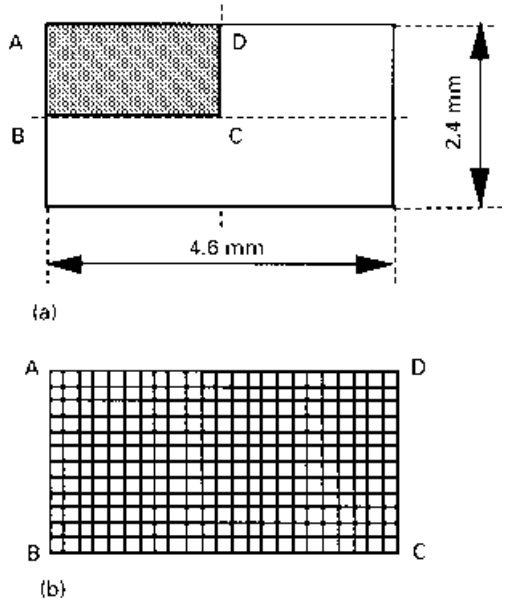

Figure 5 An analysis model for FEM: (a) analysis region; (b) mesh subdivision. The width and thickness of the specimen are 4.6 mm and 2.4 mm, respectively. The quenching surfaces are AB and AD where the value of h is constant.

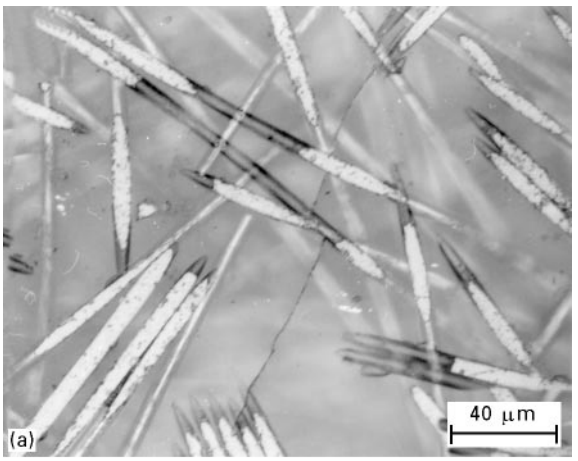

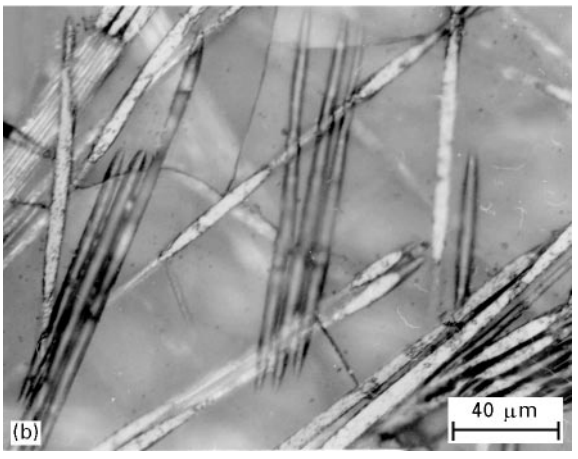

Figure 6 Optical micrographs of thermal-shock-induced matrix cracking at (a) $\Delta T = 530\,\mathrm{K}$ and (b) $\Delta T = 600\,\mathrm{K}$.

On the other hand, only a "knee" point can be seen in the stress–strain curve for plate 611 with pre-cracks. Plate 634 with thermal shock damage ($\Delta T = 600\,\mathrm{K}$) does not show the three-stage stress–strain behaviour

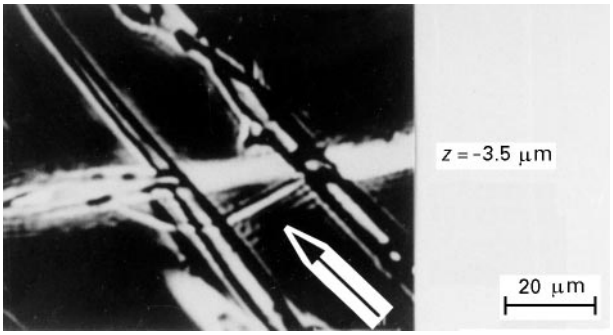

Figure 7 A scanning acoustic micrograph of matrix cracking induced by thermal shock. Multiple interference fringes (arrow) indicate the matrix crack.

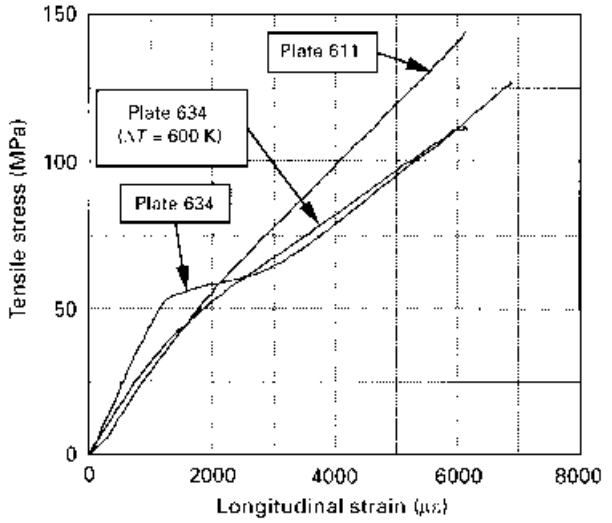

Figure 8 Stress–strain curves for the plate 611, the virgin plate 634 and the thermally shocked plate 634 specimens. με, 10^{-6} mm/mm.

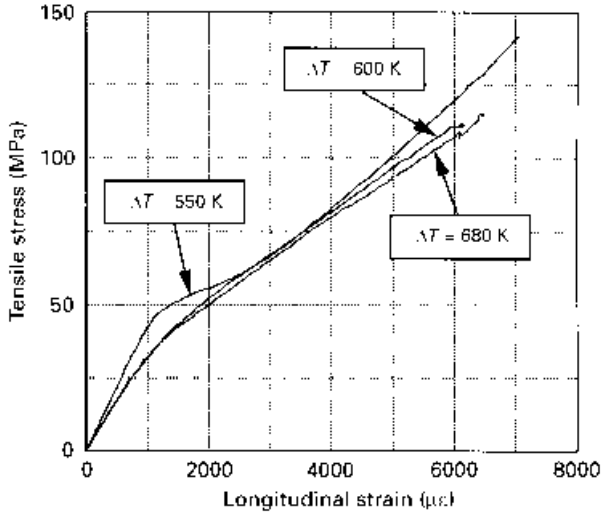

Figure 9 Effect of temperature difference on tensile stress–strain curves of plate 634 specimens. με, 10^{-6} mm/mm.

and the initial Young's modulus is reduced to 34 GPa. As a result, it is proved that the entire tensile characteristics for plate 634 with thermal shock are similar to those for virgin plate 611.

Tensile stress–strain curves for thermally shocked plate 634 specimens are shown in Fig. 9 for three

different temperature differences ΔT. Tensile behaviour at $\Delta T = 530\,K$ is different from that at $\Delta T = 600\,K$ (or 660 K). Fig. 10 shows the effect of temperature difference on initial Young's modulus. The initial Young's modulus decreases significantly at $\Delta T = 550$–$600\,K$. Cumulative AE events during tensile loading are plotted in Fig. 11. The change in AE amplitude distributions for virgin plate 634, virgin plate 611 and plate 634 with thermal shock is shown in Fig. 12a, b and c, respectively. From an optical micrograph of the fracture surface (Fig. 13), it is clear that many fibres were pulled out and broken in the final failure stage of this composite material.

4.3. Replica and *in-situ* scanning acoustic microscopy observation

Fig. 14a and b show the optical micrographs of replica showing matrix microcracking in the virgin plate 634 and the virgin plate 611 specimens, respectively. The

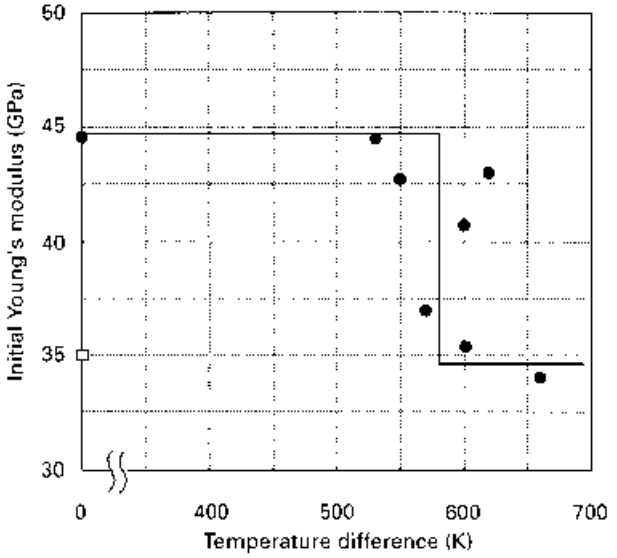

Figure 10 Change in Young's modulus against temperature difference at thermal shock. (●), plate 634; (□), plate 611.

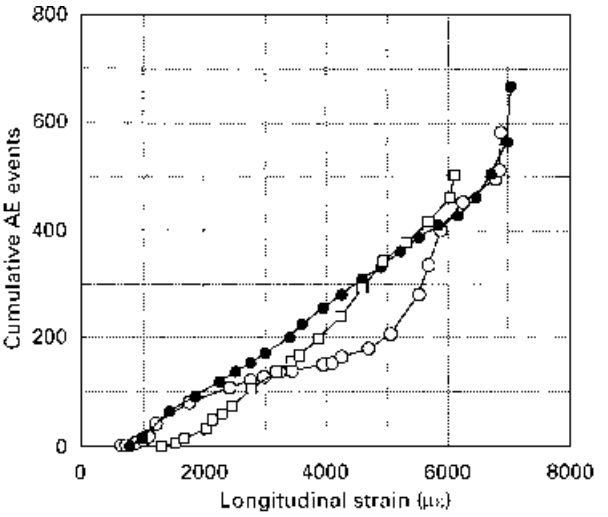

Figure 11 Cumulative AE events as a function of longitudinal strain. (●) Plate 634 ($\Delta T = 530\,K$); (○), virgin plate 634; (□), virgin plate 611. με, 10^{-6} mm/mm.

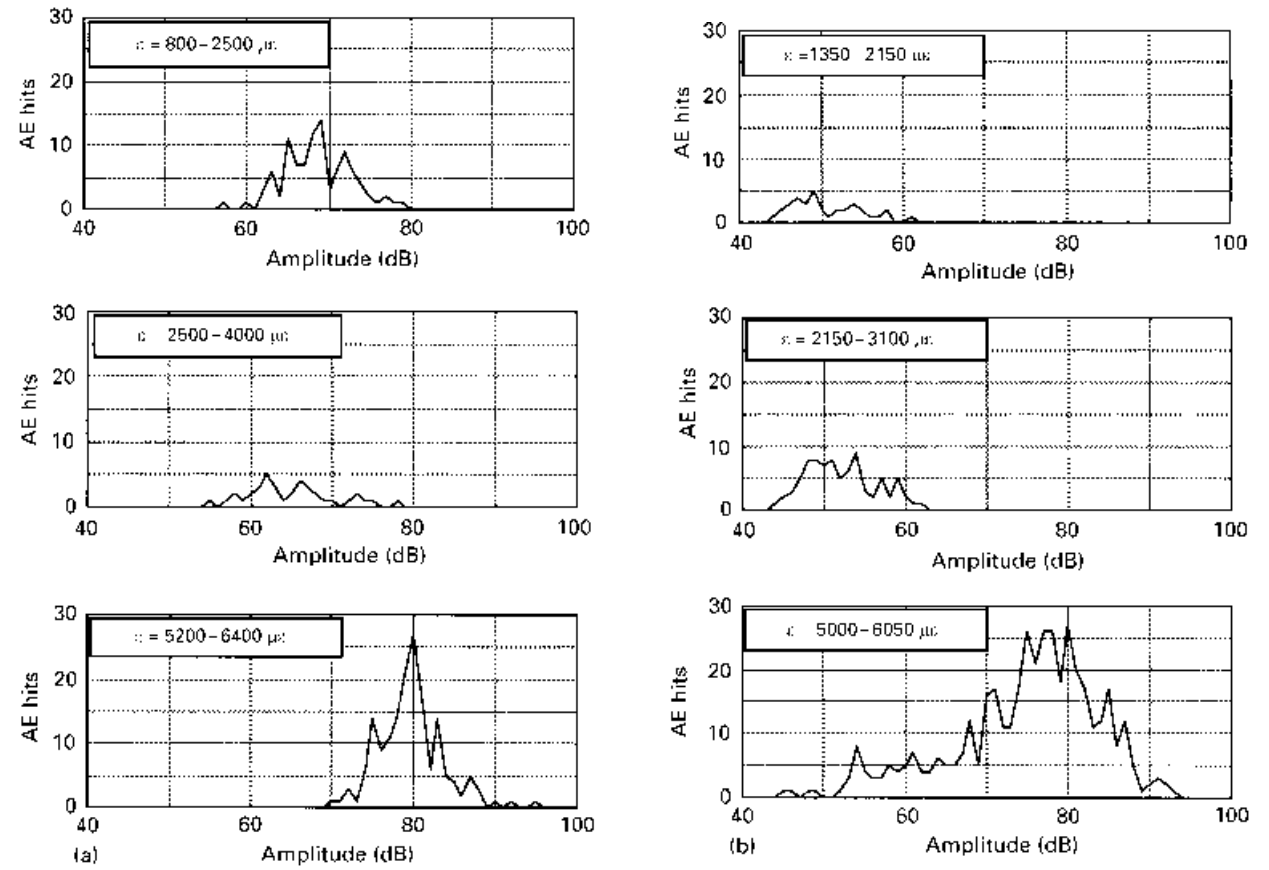

Figure 12 Change in AE amplitude distributions in (a) the virgin plate 634, (b) the virgin plate 611 and (c) the thermally shocked plate 634 specimens. με, 10^{-6} mm/mm.

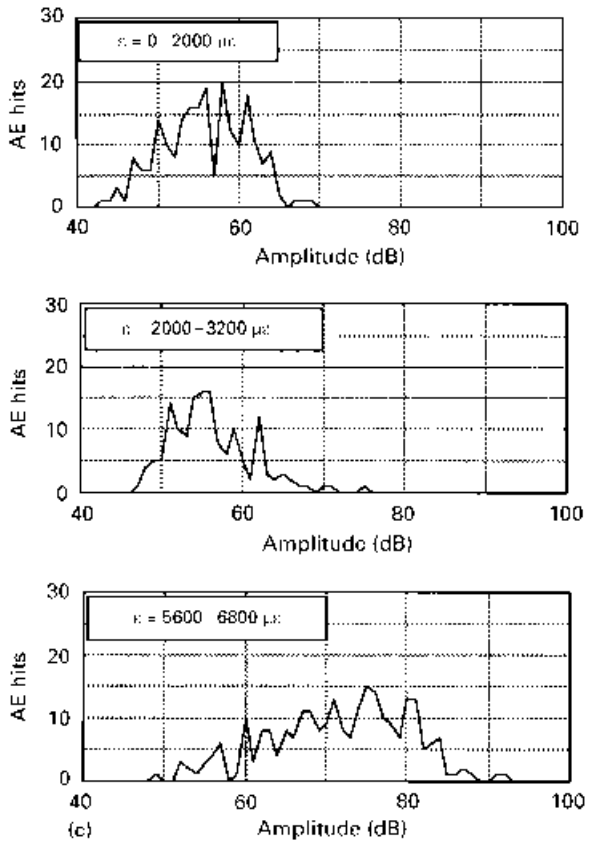

Figure 12 (Continued)

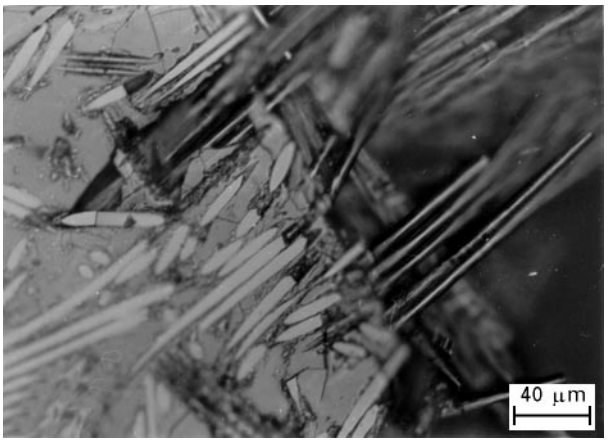

Figure 13 An optical micrograph of the fracture surface.

crack path in the virgin plate 634 is almost straight while, in the virgin plate 611, the crack lines are relatively tortuous. This is due to the difference in fracture process and, in particular, to the difference in evolution of matrix cracking. Matrix cracking in the thermally shocked plate 634 specimen is shown in Fig. 14c. The crack pattern in this specimen is zigzag and similar to that of the virgin plate 611. Fig. 15 indicates the damage progress in the thermally shocked plate 634 specimen observed *in situ* under SAM. It can be observed that thermal-shock-induced cracks ($\sigma = 0$ MPa) are connected with new cracks generated because of tensile stress.

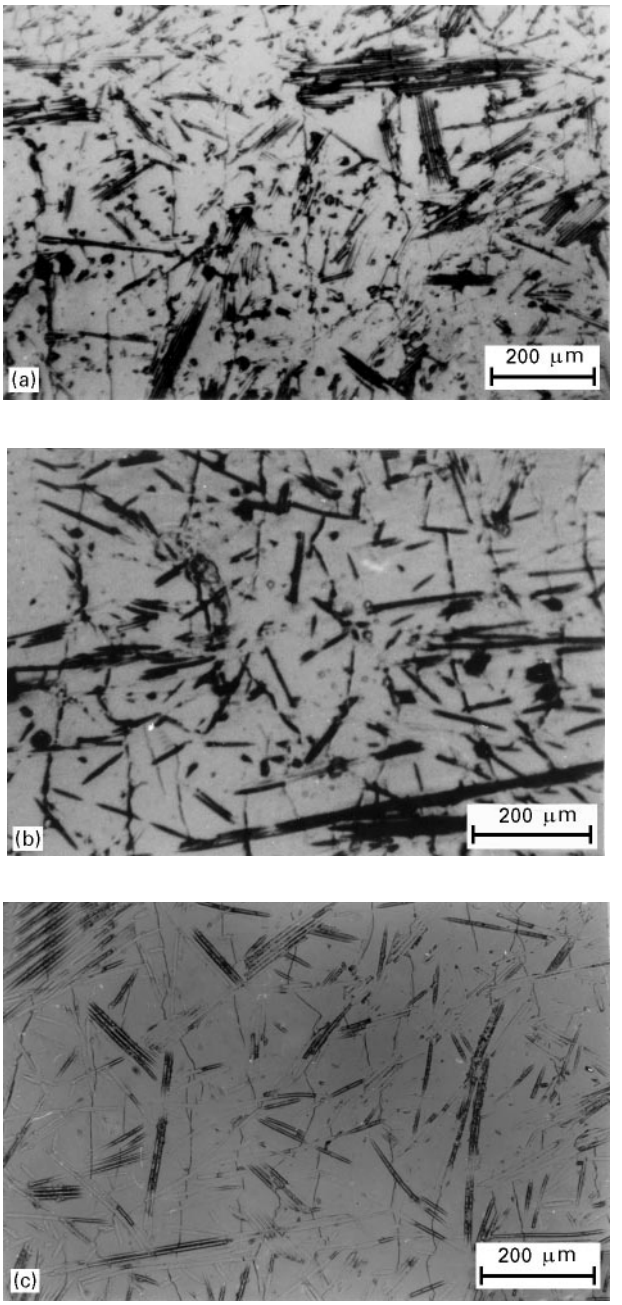

Figure 14 Optical micrographs of replica of microcracking in (a) the virgin plate 634, (b) the virgin plate 611 and (c) the thermally shocked plate 634 specimens.

4.4. Thermal stress analysis

Thermal stress distribution in the specimen quenched from 620 to 20 °C ($\Delta T = 600$ K) is presented in Fig. 16. Tensile stress is generated on the surface while compressive stress is induced inside the specimen.

Time history of the maximum thermal stress on the surface is shown in Fig. 17 for the temperature difference, $\Delta T = 600$ K, and the heat transfer coefficient, $h = 10\,000$ W m^{-2} K^{-1}. This h value corresponds to Biot's modulus, $\beta \approx 20$, which is a typical value for a water quench test. The peak value of the maximum stress is 32 MPa, which is larger than the measured ultimate matrix strength ($\sigma_{mu} = 27$ MPa) where AE begins to occur. (Note that the first matrix cracking occurs at a lower stress than 50 MPa, which is the proportional limit). This suggests that matrix cracking

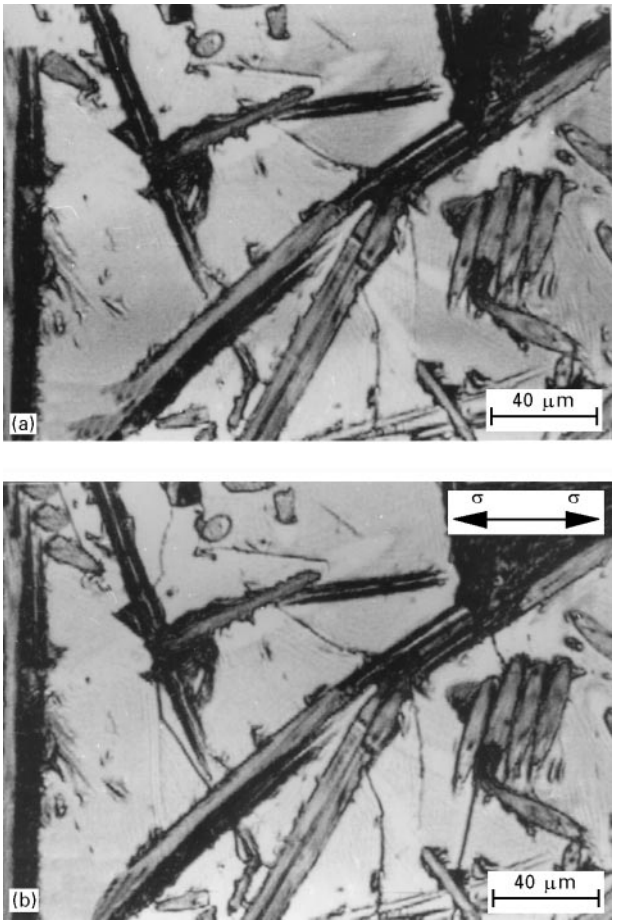

Figure 15 Progress of damage in the thermally shocked plate 634 specimen observed by *in-situ* SAM at (a) $\sigma = 0$ MPa and (b) $\sigma = 106$ MPa.

can occur if the specimen is subjected to thermal shock under these heat conditions.

5. Discussion

5.1. Tensile behaviour of the virgin plate 634

Young's modulus of a randomly oriented fibre-reinforced composite is expressed as

$$E_C = \eta E_f V_f + E_m V_m \quad (1)$$

where E and V depict Young's modulus and volume fraction, the subscripts f and m mean fibre and matrix, respectively, and η is an efficiency factor of fibre reinforcement. The efficiency η includes the effects of fibre orientation, fibre length and interfacial shear stress. Using $E_f = 234$ GPa, $E_m = 63$ GPa, $V_f = 0.30$ and $E_C = 45$ GPa (measured in the stage I), we obtain $\eta = 0.013$. This low reinforcement efficiency means that the interfacial bonding between fibre and matrix is imperfect. The radial coefficient of thermal expansion (CTE) of a fibre is much larger than that of matrix, while the axial CTE of a fibre is negative (Table I). As a result, fibres shrink away from the surrounding matrix when the CF-reinforced glass is cooled from a hot-pressing temperature. This shrinkage of fibres is expected to cause a low interfacial shear strength or a low frictional stress.

The plateau portion in stage II is due to extensive matrix cracking. An increase in longitudinal strain is

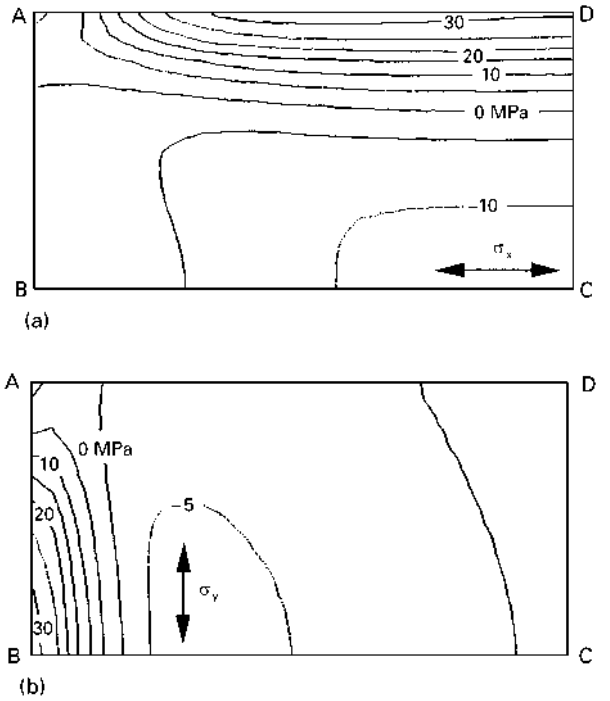

Figure 16 Thermal stress distributions in a thermally shocked specimen calculated by the FEM under the conditions $\Delta T = 600$ K, $h = 10\,000$ W m^{-2} K^{-1} and $t = 0.1$ s after quenching: (a) σ_x; (b) σ_y.

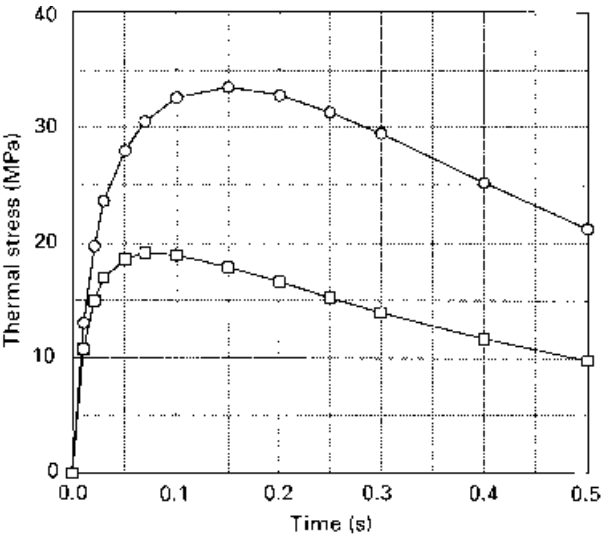

Figure 17 Time history of the maximum thermal stress on the specimen surface calculated by FEM under the conditions $\Delta T = 600$ K and $h = 10\,000$ W m^{-2} K^{-1}. (○), σ_x; (□), σ_y.

given by [17, 18]

$$\Delta\varepsilon_C = \frac{\alpha}{2}\varepsilon_{mu} \quad (2)$$

where $\alpha = E_m V_m / k E_f V_f$ (k is approximately 0.25 for short fibre reinforcement in a two-dimensional random array [19]) and ε_{mu} is matrix failure strain. The substitution of E_f, E_m and V_f values into Equation 2 yields $\Delta\varepsilon_C = 1.25\varepsilon_{mu}$. Using the measured ε_{mu} (=0.12%), we can obtain $\Delta\varepsilon_C = 0.15\%$. This value agrees well with the experimental result.

In stage III, the prediction of Young's modulus is difficult because the fracture process is complicated.

More information on the fibre–matrix interface and microscopic fracture mode is necessary to understand the stress–strain behaviour in stage III.

5.2. Comparison of tensile behaviour

The plate 634 specimen with thermal shock of $\Delta T = 530\,\mathrm{K}$ has almost the same initial Young's modulus as a virgin plate 634 specimen and shows three-stage stress-strain behaviour like virgin plate 634. In the case when $\Delta T = 600$ or 660 K, however, the initial modulus decreases considerably, and the three-stage behaviour is not observed (Fig. 9). From this result, a critical temperature difference, ΔT_c, where the initial modulus decreases rapidly, can be determined as about 550–600 K (Fig. 10).

It is well known that the significant strength degradation occurs when the specimen is damaged to some critical degree. The strength and initial modulus can be predicted using the crack density. Acoustic surface wave velocities measured by SAM changed appreciably after the thermal shock, which proves that the elastic modulus near the surface decreases with an increase in the crack density. Quantitative SAM measurement of acoustic wave velocities is now under study.

5.3. Acoustic emission characteristics and matrix crack evolution

Tensile behaviour is also characterized by AE analysis. The change in cumulative AE events for the thermally shocked plate 634 specimen is similar to that for the 611 specimen. In both specimens, the cumulative AE events increase monotonically (Fig. 11). In the virgin plate 634 specimen, the rate of AE events decreases when the matrix crack density is saturated, which corresponds to the end of stage II in the stress–strain curve.

The similarity between thermally shocked plate 634 and plate 611 is also observed in the AE amplitude distributions. That is, the amplitudes except near the final failure stage range from 45 to 65 dB both in Fig. 12b and in Fig. 12c. This is smaller than the amplitudes ranging from 60 to 80 dB in Fig. 12a. Small-amplitude AE signals in both the plate 611 and the thermally shocked plate 634 specimens are generated when pre-existing microcracks randomly distributed in matrix coalesce and propagate to produce major cracks. On the contrary, the large-amplitude AE in the virgin plate 634 specimen is generated when the matrix cracking occurs through the width and normal to the tensile direction. It is concluded that the above difference in AE characteristics results from a difference in the fracture processes. Replica observation of the progress of damage during tensile loading confirms this conclusion. The matrix crack pattern for the thermally shocked plate 634 specimen is analogous to that for the virgin plate 611 specimen (Fig. 14).

5.4. Modelling of the fracture processes

To summarize the above discussion, the difference in fracture processes is schematically shown in Fig. 18. In the virgin plate 634, extensive matrix cracking occurs at stage II. After the matrix cracking saturates, the final failure occurs with fibre pull-out and fibre fracture. In the virgin plate 611 with pre-cracks (or the thermally shocked plate 634 with initial damage), on the other hand, the pre-cracks (or the thermal-shock-induced cracks) continuously coalesce and propagate to the final failure.

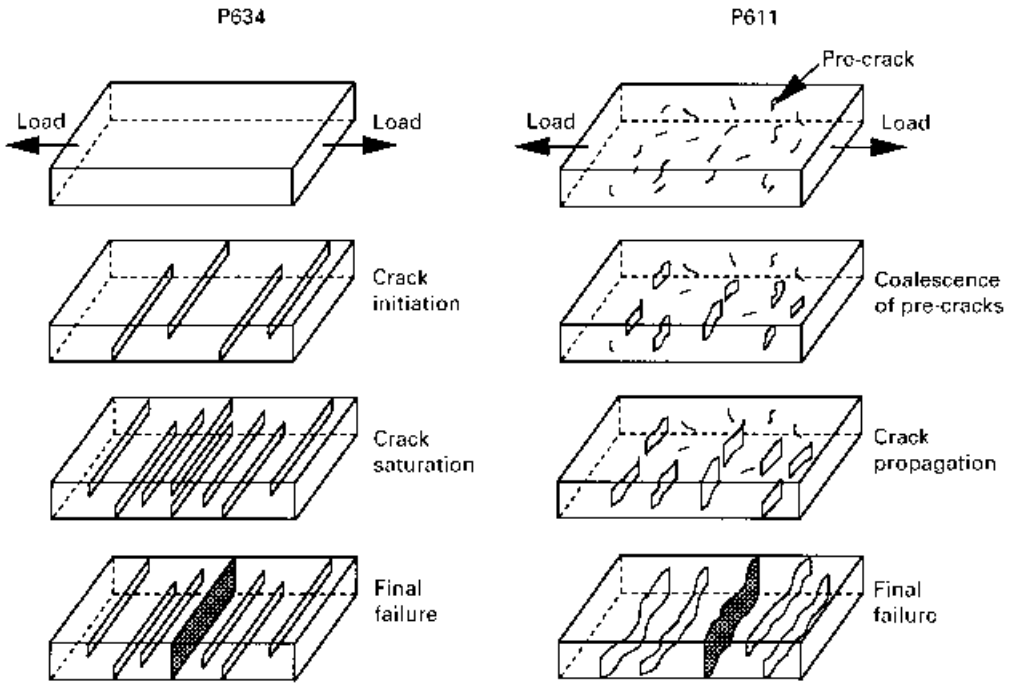

Figure 18 Schematic illustration of the difference in fracture processes for plate 634 and plate 611 (or thermally shocked plate 634) specimens.

6. Conclusions

Microfracture processes of randomly oriented discontinuous CF-reinforced glass matrix composites with and without thermal shock were characterized by microscopic observations and AE analysis. The conclusions are as follows:

1. Thermal-shock-induced damage was examined using optical microscopy and SAM. In particular, SAM is most suitable for the observation of matrix cracks existing near the surface.

2. The replica and *in-situ* SAM techniques permit microscopic observation of matrix cracking evolution.

3. The fracture processes of thermally shocked plate 634 was found to be similar to that of plate 611 through comparison of stress–strain curves and AE behaviours and by microscopic observation of matrix cracking.

4. The difference in the tensile behaviours and AE properties of the virgin and the thermally shocked plate 634 specimens is attributed to the difference in the fracture processes. That is, the presence of initial cracks affects the failure modes and in particular, matrix cracking patterns and evolution.

References

1. A. G. EVANS and F. W. ZOK, *J. Mater. Sci.* **29** (1994) 3857.
2. S.-W. WANG and A. PARVIZI-MAJIDI, *ibid.* **27** (1992) 5483.
3. P. G. KARANDIKAR and T.-W. CHOU, *Compos. Sci. Technol.* **46** (1993) 253.
4. D. S. BEYERLE, S. M. SPEARING, F. W. ZOK and A. G. EVANS, *J. Amer. Ceram. Soc.* **75** (1992) 2719.
5. D. S. BEYERLE, S. M. SPEARING and A. G. EVANS, *ibid.* **75** (1992) 3321.
6. I. M. DANIEL, G. ANASTASSOPOULOS and J.-W. LEE, *Compos. Sci. Technol.* **46** (1993) 105.
7. A. DALMAZ, P. REYNAUD, D. ROUBY and G. FANTOZZI, *J. Mater. Sci.* **31** (1996) 4213.
8. S. M. BLEAY, B. HARRIS, V. D. SCOTT, R. G. COOKE and F. A. HABIB, *ibid.* **31** (1996) 5933.
9. H. TSUDA, J. TAKAHASHI, K. KEMMOCHI and R. HAYASHI, *J. Amer. Ceram. Soc.* **79** (1996) 2293.
10. Y. KAGAWA, N. KUROSAWA and T. KISHI, *J. Mater. Sci.* **28** (1993) 735.
11. H. WANG and R. N. SINGH, *J. Amer. Ceram. Soc.* **79** (1996) 1783.
12. J. E. WEBB and R.N. SINGH, *ibid.* **79** (1996) 2857.
13. M. J. BLISSETT, P. A. SMITH and J. A. YEOMANS, *J. Mater. Sci.* **32** (1997) 317.
14. K. M. PREWO, *ibid.* **17** (1982) 3549.
15. N. TAKEDA, O. CHEN, T. KISHI, W. K. TREDWAY and K. M. PREWO, *Engng Fract. Mech.* **40** (1991) 791.
16. N. TAKEDA, C. MIYASAKA and K. NAKATA, *Nondestr. Test. Eval.* **8–9** (1992) 813.
17. J. AVESTON, R. A. MERCER and J. M. SILLWOOD, National Physical Laboratory Report SI-90-11-98 (1975).
18. J. AVESTON, A. KELLY, *J. Mater. Sci.* **8** (1973) 352.
19. V. LAWS, *J. Phys. D*, **4** (1971) 1737.

Received 2 April
and accepted 29 May 1997